JOURNAL OF THERMOPHYSICS AND HEAT TRANSFER
Vol. 15, No. 2, April–June 2001

Application of Planck–Rosseland–Gray Model for High-Enthalpy Arc Heaters

Takeharu Sakai* and Keisuke Sawada†
Tohoku University, Sendai 980-8579, Japan
and
Masahiko Mitsuda‡
Kobe Steel Ltd., Hyogo 651-2271, Japan

The existing ARCFLO computer code for numerically simulating the flow in the constrictor of a constricted-arc wind tunnel is upgraded by replacing the two-band gray-gas radiation model with the Planck–Rosseland–Gray model developed recently. The code is now applicable to both air and carbon dioxide flows. For the airflows thermochemical nonequilibrium is accounted for approximately in determining the thermodynamic variables. For the carbon dioxide flows condensation of solid carbon on the wall is accounted for. Turbulence parameters are adjusted to accommodate the change in the radiation model. For airflows the present modification reproduces the existing experimental data well. For carbon dioxide flows the present code predicts operating characteristics that are similar to those for airflows and a thin carbon deposit layer on the wall.

Nomenclature

a_t = coefficient of the mixing length
B_λ = blackbody (Planck) function at given wavelength λ, W/(cm^2-sr-μm)
D = constrictor diameter, cm
$\mathcal{D}$ = binary diffusion coefficient, cm^2/s
D_n = exponential integral function of order n
dl = carbon layer thickness, cm
E_i = ionization potential of species i, erg
H_{av} = mass-averaged enthalpy, MJ/kg
I = current, A
I_λ = radiation intensity at given wavelength λ, W/(cm^2-sr-μm)
K_s = equivalent sand grain roughness height, m
k = Boltzmann constant, 1.3806×10^{-23} J/K, or thermal conductivity, W/(m-K)
L = constrictor length, cm
$\dot{m}$ = mass-flow rate, kg/s
m_i = mass of species i, kg
N_i = number density of species i, cm^{-3}
p = pressure, atm
q_r = radiative heat flux, W/cm^2
q_r^+ = radiative heat flux directed away from a given point r, W/cm^2
q_r^- = radiative heat flux directed toward a given point r, W/cm^2
q_w = total heat flux at wall, W/cm^2
R = constrictor radius, cm
R_u = universal gas constant, J/(kg-mol-K)
r = radial distance, cm
T = heavy particle temperature, K
T_e = electron temperature, K
v = velocity, cm/s
Z = axial distance, m
α = angle
α_{eq} = ionization fraction at equilibrium
α_w = ionization fraction at wall
γ = angle
θ = angle
κ_λ = absorption coefficient at given wavelength including stimulated emission, cm^{-1}
λ = wavelength, μm
ν = kinematic viscosity, m^2/s, or frequency, s^{-1}
ρ = density, kg/m^3
τ = shear stress, N/m^2

Subscripts

e = electron
eff = effective wall value
eq = equilibrium point
G = Gray-gas mean
P = Planck mean
R = Rosseland mean
w = wall

Presented as Paper 98-2838 at the AIAA/ASME 7th Joint Thermophysics and Heat Transfer Conference, Albuquerque, NM, 15–18 June 1998; received 29 March 2000; revision received 24 October 2000; accepted for publication 25 October 2000.

*Graduate Student, Department of Aeronautics and Space Engineering, Aobayama01; currently NRC Research Associate, NASA Ames Research Center, Mail Stop 230-2, Reacting Flow Environments Branch, Moffett Field, CA 94035.

†Professor, Department of Aeronautics and Space Engineering, Aobayama01. Senior Member AIAA.

‡Senior Researcher, Mechanical Engineering Research Laboratory, Takatsukadai, Nishi-ku. Member AIAA.

Introduction

DEVELOPING reliable heatshields for spacecrafts is a prerequisite to the success of a space mission. The heatshield of a space vehicle is exposed to a high-enthalpy environment during an atmospheric entry. One of the facilities that can produce such an environment is the segmented constrictor type arc-heated wind tunnel. This type of arcjet wind tunnel has been developed since the late 1950s in the United States.[1] In Japan, with increasing attention to space activities, such a facility was first installed in the early 1990s (see, e.g., Ref. 2).

The constricted-arc-type wind tunnel consists of four main components. They are as follows: the upstream electrode chamber, the constrictor tube, the downstream electrode chamber, and the convergent-divergent nozzle. A computer code named ARCFLO has been developed to calculate the flow in the constrictor tube.[3,4] The code is used as a tool in the design of such a facility. In this code the so-called parabolized Navier–Stokes-type equations are solved.

Several assumptions are made in this code in modeling physical phenomena.

Of these assumptions the one concerning radiation is the most crucial because energy transfer occurs mostly by radiation. The existing ARCFLO code employs a simplified two-band Gray-gas model.[4] The two Gray-gas parameters are selected in such a way that the overall operating characteristics of the tunnel, that is, those regarding electrical voltage and current and wall heating rate, are correctly reproduced. With the existing ARCFLO code only a few seconds of computing time is needed for calculating one operating condition using this radiation model. Good agreement is seen between the ARCFLO calculation and experimental data.[2,4] Such a good agreement is a result of appropriate choice of the two absorption coefficients. Such a choice is arrived at through a long series of trials and errors involving experiments. In the typical operating condition of such a wind tunnel, however, the optical depth varies over such a wide range that Gray-gas description is theoretically impossible. Therefore, the Gray-gas parameters so chosen have little rational basis.

The thermodynamic state of the flow in the constrictor is not calculated accurately by the ARCFLO code because of the empirical approach made in the radiation model. The uncertainty in the thermodynamic state leads to an uncertainty in the flow properties in the test section and ultimately to an uncertainty in the performance of the heatshield materials tested in the tunnel. A better radiation model is needed in order to calculate the flow properties more accurately.

In the existing ARCFLO code radiative transfer is calculated only in the radial direction. The existing two-band model is adjusted to reproduce the experimentally observed radial heat-transfer rates. In the future, one may attempt to calculate radiative transfer in the axial direction to determine the properties of the gas flow, for instance, at the throat of the nozzle. Because there are no experimental data for the axial radiative transfer phenomenon, such calculation must be made using a radiation model based on the first principles. The existing two-band model is inadequate for this purpose.

The ARCFLO code is presently capable of analyzing only air. This is because experimental data exist only for air. When a space vehicle enters into the atmosphere of Mars and Venus, the shock layer over a reentry vehicle contains carbonaceous species. To test the heatshields to be used in such atmospheres, an arc-heated wind tunnel must be operated with a working gas containing carbon. The two absorption coefficients in the existing ARCFLO code for a carbonaceous gas then need to be empirically determined. It is desirable to avoid such a trial-and-error process. For that purpose an ab initio radiation model is preferred.

For an accurate radiation calculation line-by-line calculation is most desirable. However, computing time for such a calculation is prohibitively large. A theoretical model named Planck–Rosseland–Gray (PRG) model has recently been developed for the purpose of simplifying radiative transport calculations.[5] The PRG model calculates radiative heat fluxes using three mean absorption coefficients, which are the Planck, Rosseland, and Gray-gas means. This model, based on the fundamental principles of radiative transfer, can closely reproduce the radiative heat-flux values obtained by a detailed line-by-line calculation for a one-dimensional radiating field.[5,6] If the two-band model in ARCFLO code can be replaced by the PRG model, an accurate prediction of arc-heater performance will become possible without carrying out the trial-and-error procedure.

The purpose of the present study is to upgrade the ARCFLO code by incorporating the PRG model. The upgraded ARCFLO code is first tested against the existing experimental data for air. The test necessitated changing the turbulence model employed in the code. In the existing ARCFLO code the turbulence parameters are so chosen as to be compatible with the two-band radiation model used. When a rational radiation model is used, the turbulence model must be changed accordingly. Second, the upgraded ARCFLO code is applied for a carbon-dioxide (CO_2) flow for which experimental data do not exist. The turbulence parameters that reproduce the experimental data for air are used for the carbonaceous gas.

To adapt the ARCFLO code to a carbonaceous working gas, three problems must be overcome. The first is the radiation model. In the Martian and Venusian atmospheres, mainly atomic carbon (C), atomic oxygen (O), and carbon-monoxide (CO) contribute to radiation.[7] The accuracy of the PRG model has already been shown for such a case.[5] The second problem concerns the transport properties. In the ARCFLO code they are calculated using Yos' formulation.[4] Similar collision integrals are generated for the carbonaceous species in the present work. The third problem concerns wall boundary conditions. When carbonaceous test gas is used in the constricted arc, atomic carbon condenses on the wall. Therefore, the effective wall temperature is that of this carbon layer surface. This problem is addressed in the present work.

Method of Calculation

Radiative Heat Flux

The mathematical description of radiative transport in cylindrical coordinates is well known (see, e.g., Refs. 4 and 8). Therefore, only its essence is presented here. The governing equation for radiative transfer is given by

$$\frac{\mathrm{d}I_\lambda}{\mathrm{d}s} = \kappa_\lambda (B_\lambda - I_\lambda) \tag{1}$$

where I_λ is the intensity of radiation traveling along a ray s, κ_λ is an absorption coefficient, B_λ is the Planck function. For the cylindrical geometry shown in Fig. 1, the radiative heat flux at a given r is determined by

$$q_\lambda(r) = \int I_\lambda(r) \cos\theta \, \mathrm{d}\Omega \tag{2}$$

Integrating Eq. (1) and substituting it into Eq. (2), the radiative heat flux is written in the following form[4,8]:

$$q_\lambda(r) = q_\lambda^+(r) + q_\lambda^-(r) \tag{3}$$

where $q_\lambda^+(r)$ is the radiative heat flux directed away from the point r and $q_\lambda^-(r)$ is the radiative heat flux directed toward the point r. They are given by the following equations:

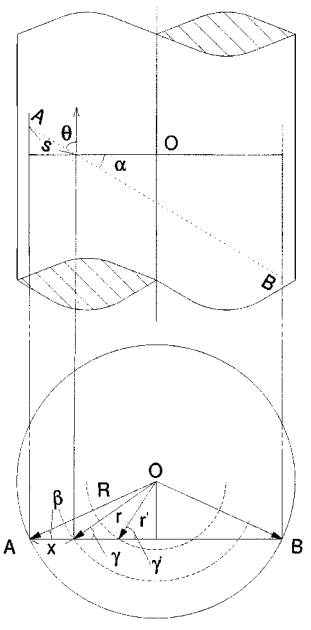

Fig. 1 Cylindrical geometry.

$$q_\lambda^+(r) = 4\int_0^{\pi/2}\left[B_\lambda(R)D_3\left(\int_0^{r\cos\gamma}\kappa_\lambda\,\mathrm{d}y + \int_0^{\sqrt{R^2-r^2\sin^2\gamma}}\kappa_\lambda\,\mathrm{d}y\right)\right.$$
$$+\int_0^{r\cos\gamma}\kappa_\lambda B_\lambda D_2\left(\int_y^{r\cos\gamma}\kappa_\lambda\,\mathrm{d}y'\right)\mathrm{d}y$$
$$+\int_0^{\sqrt{R^2-r^2\sin^2\gamma}}\kappa_\lambda B_\lambda D_2\left(\int_0^{r\cos\gamma}\kappa_\lambda\,\mathrm{d}y'\right.$$
$$\left.\left.+\int_0^{y}\kappa_\lambda\,\mathrm{d}y'\right)\mathrm{d}y\right]\cos\gamma\,\mathrm{d}\gamma \tag{4}$$

and

$$q_\lambda^-(r) = -4\int_0^{\pi/2}\left[B_\lambda(R)D_3\left(\int_{r\cos\gamma}^{\sqrt{R^2-r^2\sin^2\gamma}}\kappa_\lambda\,\mathrm{d}y\right)\right.$$
$$\left.+\int_{r\cos\gamma}^{\sqrt{R^2-r^2\sin^2\gamma}}\kappa_\lambda B_\lambda D_2\left(\int_{r\cos\gamma}^{y}\kappa_\lambda\,\mathrm{d}y'\right)\mathrm{d}y\right]\cos\gamma\,\mathrm{d}\gamma \tag{5}$$

where

$$y = \sqrt{r'^2 - r^2\sin^2\gamma}, \qquad y' = \sqrt{r'^2 - r^2\sin^2\gamma}$$

$$D_n(z) = \int_0^1 \frac{\mu^{n-1}}{\sqrt{1-\mu^2}}\exp\left(-\frac{z}{\mu}\right)\mathrm{d}\mu$$

In the PRG model an absorption coefficient at a given wavelength point at a given cell in a flowfield is classified into one of the Planck, Rosseland, and Gray-gas means. The classification is achieved by using a selection criterion.[9,10] In the present study the classification is conducted as follows: for the optically thin criterion

$$\kappa_\lambda \Delta r < \Delta\tau_P \tag{6}$$

For the optically thick criterion

$$\kappa_\lambda \Delta r < \Delta\tau_R \tag{7}$$

where $\Delta\tau_P$ and $\Delta\tau_R$ denote selection criteria.[5] For the in-between cases the absorption coefficient is classified into the Gray-gas means. Then, three mean absorption coefficients are obtained in each group, and the radiative heat fluxes are computed in each group. Each of the radiative heat fluxes for the present cylindrical geometry is given respectively as

$$q_P = q_P^+ - q_P^- \tag{8}$$

$$q_R = q_R^+ - q_R^- \tag{9}$$

$$q_G = q_G^+ - q_G^- \tag{10}$$

where

$$q_P^+ = 4\int_0^{\pi/2}\left[\frac{\pi}{4}B_P(R) + \int_0^{r\cos\gamma}\kappa_P B_P\,\mathrm{d}y\right.$$
$$\left.+\int_0^{\sqrt{R^2-r^2\sin^2\gamma}}\kappa_P B_P\,\mathrm{d}y\right]\cos\gamma\,\mathrm{d}\gamma \tag{11}$$

$$q_P^- = 4\int_0^{\pi/2}\left[\frac{\pi}{4}B_P(R) + \int_{r\cos\gamma}^{\sqrt{R^2-r^2\sin^2\gamma}}\kappa_P B_P\,\mathrm{d}y\right]\cos\gamma\,\mathrm{d}\gamma \tag{12}$$

$$q_R^+ = \int_0^{\pi/2}\left[\pi B_R(R) - \frac{8}{3}\frac{1}{\kappa_R}\frac{\mathrm{d}B_R}{\mathrm{d}T_e}\frac{\mathrm{d}T_e}{\mathrm{d}y}\right]\cos\gamma\,\mathrm{d}\gamma \tag{13}$$

$$q_R^- = \int_0^{\pi/2}\left[\pi B_R(R) + \frac{8}{3}\frac{1}{\kappa_R}\frac{\mathrm{d}B_R}{\mathrm{d}T_e}\frac{\mathrm{d}T_e}{\mathrm{d}y}\right]\cos\gamma\,\mathrm{d}\gamma \tag{14}$$

$$q_G^+(r) = 4\int_0^{\pi/2}\left[B_G(R)D_3\left(\int_0^{r\cos\gamma}\kappa_G\,\mathrm{d}y + \int_0^{\sqrt{R^2-r^2\sin^2\gamma}}\kappa_G\,\mathrm{d}y\right)\right.$$
$$+\int_0^{r\cos\gamma}\kappa_G B_G D_2\left(\int_y^{r\cos\gamma}\kappa_G\,\mathrm{d}y'\right)\mathrm{d}y$$
$$+\int_0^{\sqrt{R^2-r^2\sin^2\gamma}}\kappa_G B_G D_2\left(\int_0^{r\cos\gamma}\kappa_G\,\mathrm{d}y'\right.$$
$$\left.\left.+\int_0^{y}\kappa_G\,\mathrm{d}y'\right)\mathrm{d}y\right]\cos\gamma\,\mathrm{d}\gamma \tag{15}$$

and

$$q_G^-(r) = -4\int_0^{\pi/2}\left[B_G(R)D_3\left(\int_{r\cos\gamma}^{\sqrt{R^2-r^2\sin^2\gamma}}\kappa_G\,\mathrm{d}y\right)\right.$$
$$\left.+\int_{r\cos\gamma}^{\sqrt{R^2-r^2\sin^2\gamma}}\kappa_G B_G D_2\left(\int_{r\cos\gamma}^{y}\kappa_G\,\mathrm{d}y'\right)\mathrm{d}y\right]\cos\gamma\,\mathrm{d}\gamma \tag{16}$$

where the values denoted by the subscripts P, R, and G refer to the Planck, Rosseland, and Gray-gas part of the PRG model. The derivation of Planck and Rosseland approximation is shown in Ref. 11.

To construct the mean absorption coefficients in the PRG model, the multiband calculation is carried out. The mean absorption coefficients are determined to replicate the radiative heat-flux values of the multiband calculation. In determining the mean absorption coefficients, an iteration scheme is used to evaluate an appropriate value of τ_P (Ref. 6). In the present study the value of $\Delta\tau_R$ is fixed to a given value. The iteration is repeated up to 20 times. For the upstream region of the constrictor, in which radiation is very strong, this iteration scheme works well. However, the iteration shows a deficiency in the downstream region. This results in a small difference of the radiative heat-flux value between the PRG model and the multiband model as is shown later.

In the ARCFLO code Eqs. (4) and (5) are solved using a recursive relation.[4] The multiband calculation is carried out using the modified version of this subroutine. The modification is made in spectral integration. The equations for the Gray-gas approximation of the PRG model, Eqs. (15) and (16), are solved with this subroutine. The equations for the Planck and Rosseland approximation, from Eqs. (11–14), are discretized by using the radial mesh system employed in the ARCFLO. The total radiative heat flux in the PRG model is given by

$$q_{\mathrm{PRG}} = q_{\mathrm{PRG}}^+ - q_{\mathrm{PRG}}^- \tag{17}$$

where

$$q_{\mathrm{PRG}}^+ = q_P^+ + q_R^+ + q_G^+ \tag{18}$$

$$q_{\mathrm{PRG}}^- = q_P^- + q_R^- + q_G^- \tag{19}$$

The numerical procedure in ARCFLO is a space-marching finite difference scheme for mass, momentum, and energy conservation equations. To incorporate the PRG model into the ARCFLO code, the following procedure is taken. First, the radiative heat fluxes of

each radial point at the most upstream axial station are calculated with the multiband model. At this time the criteria for the PRG model are constructed to replicate the radiative heat-flux values of the multiband model by an iteration scheme. The parametric criteria in the PRG model need to be reconstructed if the flow properties at a downstream axial station change substantially. If temperature at a radial point at a given axial station changes 5% compared with the upstream axial station, the criteria are updated.

Calculation of Electron Temperature for Air

The radiative properties for air are relatively well known. Therefore, for air, accurate description of the thermodynamic state is warranted. In contrast, for CO_2, for which radiation properties are less accurately known, a less accurate description is allowed.

The radiation properties are determined mostly by electron temperature, which in general is different from heavy particle temperature. For air, electron temperature is determined accounting for thermal nonequilibrium. When thermal conduction in electron gas is negligible, electron temperature satisfies the relationship[10,12]

$$3m_e k N_e (T - T_e) \sum_{i=\text{ion}} \frac{\nu_i}{m_i} - \sum_{i=\text{ion}} E_i \left(\frac{\partial N_i}{\partial t} \right) = 0 \qquad (20)$$

The first term represents the rate of energy transfer to electron gas from the heavy particle gas through the elastic collisions. The second term represents the rate of energy removal through electron-impact ionization reaction. The collision frequency ν is given by the Spitzer's formula.[13] By knowing the species concentrations, Eq. (20) can be solved for T_e. Equation (20) is valid not only in the core region where flow is nearly inviscid, but also at and near the wall where the insulation effect[12] ($\partial T_e/\partial r = 0$) precludes the conduction effect.

In the core region, where the flow is mostly inviscid, the species concentration is determined by using the equilibrium relationship evaluated at p and T (Refs. 14 and 15). Near the wall, viscous diffusion is dominant, and therefore the equilibrium procedure cannot be used. In this region electron density and temperature are determined as follows: first, the outer edge of the core, expressed with a subscript eq, is determined to be the position where T_e determined from Eq. (20) is equal to (to within 3%) T. In the region from this point to the wall, which is dominated by viscous diffusion, electron density is described by a parabola, which is a solution to a simplified diffusion equation. The wall value of electron density is calculated from the conservation relationship at the wall:

$$|(\rho v)_w| \alpha_w = 2(\rho \mathcal{D}^+)_w \left| \left(\frac{\partial \alpha}{\partial r} \right)_w \right| \qquad (21)$$

where $\mathcal{D}^+$ denotes binary diffusion coefficient for ionized species. The numeric 2 accounts for the ambipolar diffusion effect.[12] Equation (21) can be written as

$$v_w \alpha_w = 2 \frac{\alpha_{\text{eq}}}{\Delta r} \mathcal{D}^+ \qquad (22)$$

where Δr denotes the distance from the equilibrium point to the wall. Therefore,

$$\frac{\alpha_w}{\alpha_{\text{eq}}} = \frac{2\mathcal{D}^+}{v_w \Delta r} \qquad (23)$$

The wall velocity v_w is about 100 cm/s (Ref. 16). The diffusion coefficient $\mathcal{D}^+$ becomes the order of 1 cm^2/s at the wall temperature of 1000 K (Ref. 17). Δr is taken to be about 1 cm. This leads to

$$\alpha_w/\alpha_{\text{eq}} \cong 0.01 \qquad (24)$$

By feeding the electron density value obtained from Eq. (24) into Eq. (20), the electron temperature at the wall is obtained. Typically, T_e at the wall is 6000 K. Such a high value of T_e results from the weak coupling between T and T_e at low degree of ionization and the fact that electron temperature is insulated from the wall.[12]

Formulation for Carbonaceous Gases

As mentioned in the Introduction, operation of an arc-heated wind tunnel with CO_2 is considered in the present work. When the wind tunnel is operated with CO_2, however, there will be a buildup of carbon deposit layer on the wall, as is discussed later. The surface of the carbon layer will be hotter than the wall. Because of the relatively low accuracy of the radiation properties for carbonaceous gas species, as is mentioned earlier, thermal nonequilibrium phenomenon is not accounted for CO_2.

CO_2 in the constrictor will dissociate and ionize, resulting in the following species: C, O, C_2, O_2, CO, CO_2, C_3, C^+, O^+, O_2^+, CO^+, and e^-. Thermochemical equilibrium is assumed, and the equilibrium thermodynamic properties of the preceding species are calculated using the free energy minimization technique.[14] To calculate transport properties, collision integrals are needed. Some of the collision integrals for the species considered in this study are given in Ref. 18 for collision pairs involving C, O, CO, O_2, or CO_2. The collision integrals among C_3, C^+, and CO^+ are assumed to be those among CO_2, C, and CO. These properties are fed into a table.

As a part of the PRG model, a multiband radiation model is first constructed for CO_2 in a way similar to that for air. The species C, O, C_2, CO, and O_2 are included in the model. The PRG model is then constructed from the multiband model.

As mentioned before, the layer of the solid carbon deposited on the wall is calculated for the CO_2 flow. The thickness of carbon layer is evaluated from the gas surface equilibrium relation: because carbon vaporizes in the form mostly of C_3, the carbon layer will grow to the thickness where its surface temperature produces equilibrium between the C_3 in the gas phase and its surface. The number density of C_3 at the flow interior point adjacent to the wall is first calculated using the equilibrium code. Next, an effective wall temperature is assumed. The equilibrium number density of the C_3 at this effective wall temperature is evaluated using the JANAF tables.[19] If the difference between the number density of C_3 in the flow and that of the equilibrium C_3 is sufficiently small, the effective wall temperature is obtained. Using this effective wall temperature, carbon layer thickness is calculated through the relation

$$q_w = k_{\text{eff}}(T_{\text{eff}} - T_w/dl) \qquad (25)$$

where k_{eff} is calculated by the form given in Ref. 20 using T_{eff} and q_w denotes the total wall heat flux. The effective wall temperature is used as the wall temperature in the radiation calculation.

Turbulence Model

Turbulence model employed in the ARCFLO code is a so-called zero-equation model. The eddy viscosity is calculated by using Prandtl's mixing length hypothesis. The mixing length is defined differently in the inner near-wall region where a wall model is valid and in the outer core region where the mixing length is proportional to the tube radius. It is expressed respectively as[4]

$$l_i = 0.4y \left[1 - \exp\left(\frac{-y\sqrt{\tau_w R_u/\rho_w}}{26\nu_w} \right) \right] \qquad (26)$$

$$l_o = a_t R \qquad (27)$$

where subscripts i and o denote an inner and an outer point, respectively, and y is the distance from the wall. The constrictor wall roughness is also modeled in the ARCFLO code. The wall roughness is evaluated by replacing y by $y + K_s$.

Calculation has shown that the original turbulence model leads to results different from the experimental data given in Ref. 4. This is because the new radiation model has emission and absorption characteristics different from the original radiation model: the new model emits in the core region and absorbs in the wall region more strongly than the original model. For this reason, in order to maintain the same degree of agreement with the experimental data, the convective component of heat transfer in the new code must be changed. This is done by changing the parameters used in the turbulence model, that is, the two parameters a_t and K_s are changed to reproduce the experimental data for airflow.

Table 1 Experimental data

Case	D, cm	L/D	$\dot{m}$, kg/s	I, A	p, atm
1	6.00	19.9	0.217	4087	6.65
2	6.00	19.9	0.176	4623	5.04
3	6.00	39.4	0.091	1070	3.87
4	6.00	39.4	0.136	2888	8.41
5	2.54	16.0	0.025	610	3.28
6	2.54	28.0	0.025	607	4.70
7	2.54	28.0	0.027	606	4.88
8	2.54	40.0	0.026	597	3.08

Table 2 Operational conditions for carbonaceous gas calculations

Case	D, cm	L/D	$\dot{m}$, kg/s	I, A	p, atm
9	6.00	20.0	0.03	1000	5.00
10	6.00	20.0	0.03	2000	5.00
11	6.00	40.0	0.03	1000	5.00
12	6.00	40.0	0.03	2000	5.00

Flow Conditions

For a dissociated or ionized test gas flow an arcjet wind tunnel must be operated at a constrictor pressure below about 10 atm.[21] Therefore, this condition is targeted in testing the new ARCFLO code with the modification in the radiation model. The experimental test conditions are given in Table 1. Of these, the cases from 1 to 4 are selected from the results obtained in the NASA Ames arcjet wind tunnel described in Ref. 4. The cases from 5 to 8 are the experimental data recently obtained at Kobe Steel in Japan.[2] The cases 5 and 6 have already reported in Ref. 2. For these cases copper electrode is used for both upstream anode and downstream cathode. Experimental details are given also in Ref. 2. Table 2 shows the hypothetical operational conditions with CO_2. The conditions other than mass flow are taken from the NASA Ames Research Center arcjet conditions for air. The mass-flow rate is taken to be relatively low to avoid a possible numerical instability in the calculation. All ARCFLO calculations are carried out by using 25 radial mesh points.

Results and Discussion

Figures 2a and 2b show the comparisons of the radiative heat-flux distributions of q_r^+, q_r^-, and q_r between the multiband model and the present model at two axial locations for case 1. The distributions of heavy particle temperature and electron temperature are also shown in these figures. It is seen that the present model reproduces the radiative heat-flux values of the multiband model quite well. Because electron energy is lost by the electron-impact ionization of atoms, electron temperature is lower than heavy particle temperature near the arc core. In contrast, electron energy is gained when the recombination reaction occurs (see the section entitled "Calculation of Electron Temperature for Air"), and therefore electron temperature is higher than heavy particle temperature near the wall. Electron temperature at the wall is about 6000 K ($R = 0.03$ m) in each case. Although not shown, the radiative heat-flux values calculated by the two-band model are lower in the core region and higher in the wall region than those by the PRG model. This difference is caused by the fact that the PRG model accounts for the stronger emission in the core and the stronger absorption in the wall than the two-band model, as stated earlier.

To obtain the solution at the constrictor exit, the PRG model is updated approximately 30 times. To know whether or not this updating cycle is adequate, calculations were carried out with the multiband model and with the PRG model. The distributions of mass-averaged enthalpy and wall heat flux are shown in Fig. 3. One can see that the mass-averaged enthalpy is not affected by the choice of radiation model. The difference in the mass-averaged enthalpy at the constrictor exit between the multiband model and the PRG model is only about 1%. The agreement of the radiative heat-flux values between the two models is good except in the downstream region.

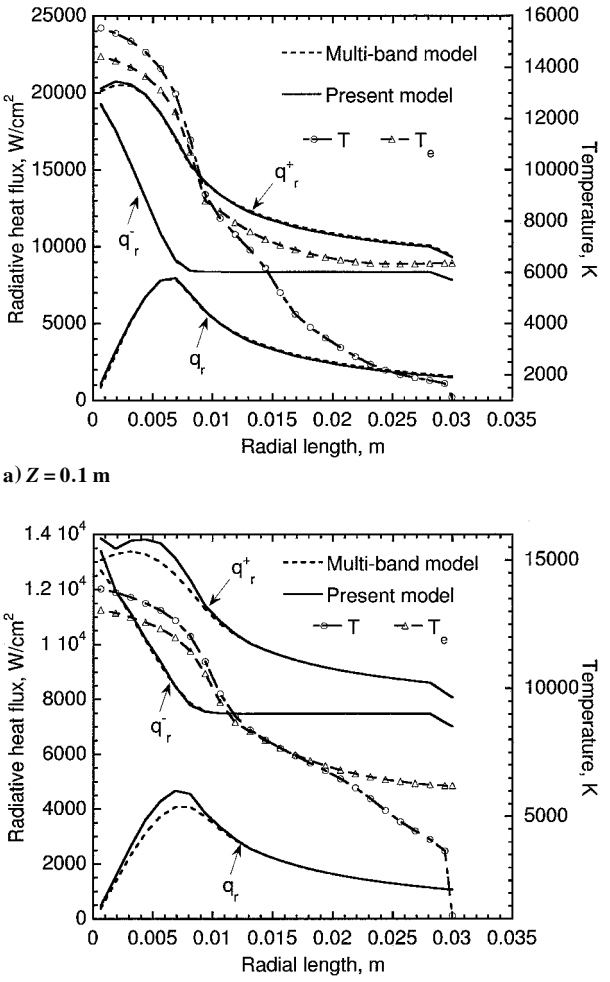

Fig. 2 Comparison of radiative heat-flux distributions between multiband model and present model and temperature distributions for case 1.

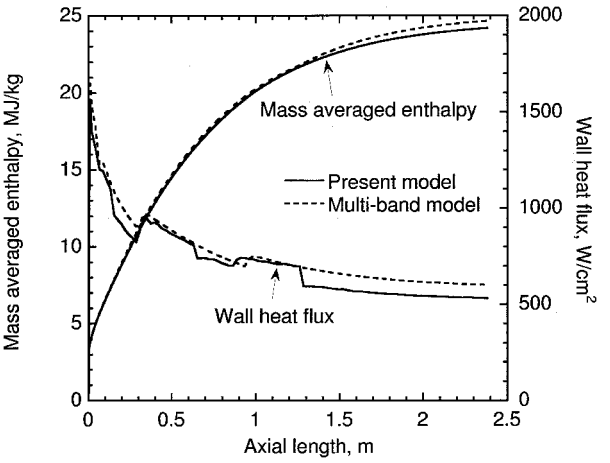

Fig. 3 Comparison of mass-averaged enthalpy and wall heat flux between multiband model and present model, case 4.

The discontinuities in the calculated wall heat-flux values by the PRG model occur because the PRG parameters are discontinuous at these points. As the figure shows, there is a small difference between the two models in the downstream region.

Comparison of the computing times for case 4 with the PRG model, that with the multiband model, and that with the two-band model of ARCFLO is given in Table 3. When the PRG model is used, the required CPU time is 50 times that of the two-band model, whereas the computation with the multiband model requires 500

Table 3 Comparison of CPU time for PRG model, multiband model, and original two-band radiation model

Radiation model	CPU time (SX-4), s
PRG	327
Multiband	3147
Two-band	7

Table 4 Comparison of mass-averaged or total enthalpy and voltage drops between experiments and ARCFLO calculations for two-band and PRG models (parenthesis show the error between the calculated and measured values)

	Measured		ARCFLO			
			Two-band		PRG	
Case	ΔV, V	H_{av}, MJ/kg	ΔV, V	H_{av}, MJ/kg	ΔV, V	H_{av}, MJ/kg
1	2727	20.5	2122 (−22.2%)	23.0 (12.2%)	2391 (−12.1%)	22.6 (10.2%)
2	2253	23.5	1925 (−14.5%)	26.5 (12.8%)	2147 (−5.0%)	26.1 (11.1%)
3	3265	16.7	3013 (−8.0%)	16.8 (0.6%)	3211 (−1.7%)	17.6 (5.4%)
4	4333	26.1	3405 (−21.4%)	23.7 (9.2%)	3763 (−13.2%)	24.6 (5.7%)
5	784	10.0	676 (−13.8%)	12.0 (20.0%)	666 (−15.1%)	12.3 (23.0%)
6	1169	16.2	1106 (−5.4%)	15.8 (−2.5%)	1072 (−8.3%)	16.0 (−1.2%)
7	1139	16.6	1155 (1.4%)	15.5 (−6.6%)	1124 (−1.3%)	15.7 (−5.4%)
8	1515	18.7	1470 (−3.0%)	18.1 (−3.2%)	1409 (−7.0%)	17.4 (−7.0%)

Table 5 Turbulence parameters

	Two-band		PRG	
Case	a_t	K_s	a_t	K_s
1	0.075	0.0001	0.050	0.0006
2	0.075	0.0001	0.050	0.0006
3	0.075	0.0001	0.050	0.0006
4	0.075	0.0001	0.050	0.0006
5	0.075	0.0002	0.060	0.00025
6	0.075	0.0002	0.060	0.00025
7	0.075	0.0002	0.060	0.00025
8	0.075	0.0002	0.060	0.00025

times the CPU time of the two-band model for this case. Although the small difference was seen in the downstream region, the computing time can be greatly reduced by using the PRG model.

The results of mass-averaged enthalpy and voltage drops calculated both by the PRG model and by the two-band model are summarized and compared with the experiments in Table 4. The turbulence parameters used in those calculations are given in Table 5. It is found that when the PRG model is used agreement becomes better if the wall turbulence is made stronger and the turbulence at the center of the tube is made weaker than in the existing ARCFLO code.

Mass-averaged enthalpy and voltage drop are compared between the two-band model and the PRG model for case 4 in Fig. 4. Calculated wall heat fluxes are shown in Fig. 5. In Fig. 4 the mass-averaged enthalpy calculated by the present method is close to the experimental value, but the voltage drop is not. This discrepancy is attributable to the neglecting of the voltage drop in the electrode region. In Fig. 5 the convective heat-flux values calculated with the PRG model are much higher than those given with the two-band model because of the stronger wall turbulence in the former. On the other hand, radiative heat-flux values calculated by the PRG model are much lower than those by the two-band model. This is because absorption

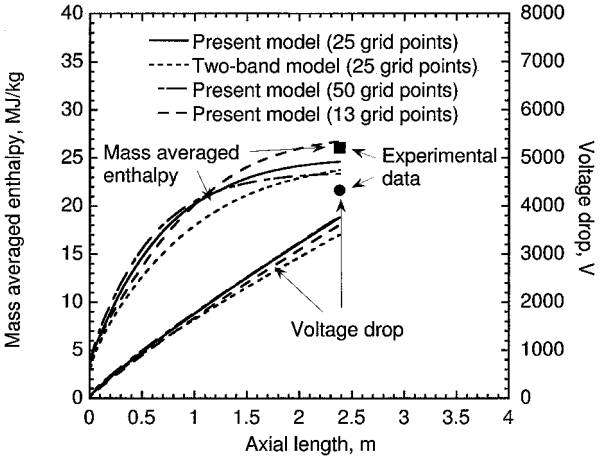

Fig. 4 Comparison of mass-averaged enthalpy and voltage drops between two-band model and present model for case 4.

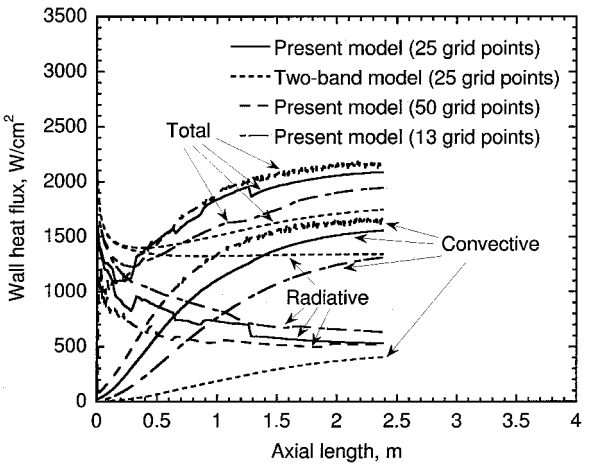

Fig. 5 Comparison of wall heat-flux distributions between two-band model and present model for case 4.

phenomenon is not fully accounted for in the two-band model. Total heat-flux values calculated by the PRG model are lower for small lift/drag (L/D) ratios than those calculated with the two band model and higher for large L/D ratios. Other cases are similar to the results presented here, though not shown.

To examine the dependence of the solution on grid, calculations are carried out for case 4. The grid refinement has been attempted in two directions, that is, the radial direction and the axial direction. For the radial direction the calculations are made using 13, 50, and 75 radial mesh points, in addition to the 25-mesh already mentioned. For the axial direction the pitch ratio (the ratio of x values between neighboring grid points in the axial direction) was changed between 1.05 and 1.005. The results for mass-averaged enthalpy and wall heat flux are shown in Figs. 4 and 5, respectively, for 13-, 25-, and 50-mesh points with the pitch ratio of 1.05. Although not shown, the results for 75-mesh points are similar to those for 50-mesh. One sees here that solutions are affected by the fineness of the grid. One can see the oscillatory behavior for 50-mesh points in the figures. When pitch ratio is decreased to 1.005, the oscillation was also seen and became more severe for the radially finer mesh. In the original ARCFLO code a 25-mesh in the radial direction and the pitch ratio of 1.05 are recommended. With the recommended mesh the present solution is free from the oscillation.

The oscillatory behavior is surmised to be caused by the interference of wall roughness with mesh: the wall roughness value used becomes too large for the calculation with a fine mesh to be realistic. Stability may be improved by changing turbulent parameters. Such improvement for the fine grid system is beyond the scope of the present work. To explore the source of the oscillation, calculation

Table 6 Calculated voltage drop and mass-averaged enthalpy for CO_2

	CO_2 flow		Airflow	
Case	ΔV, V	$\tilde{H}_{av}$, MJ/kg	ΔV, V	$\tilde{H}_{av}$, MJ/kg
9	1153	15.9	1069	17.8
10	1069	24.3	1089	26.3
11	2136	17.8	2219	20.1
12	2015	25.8	1975	28.0

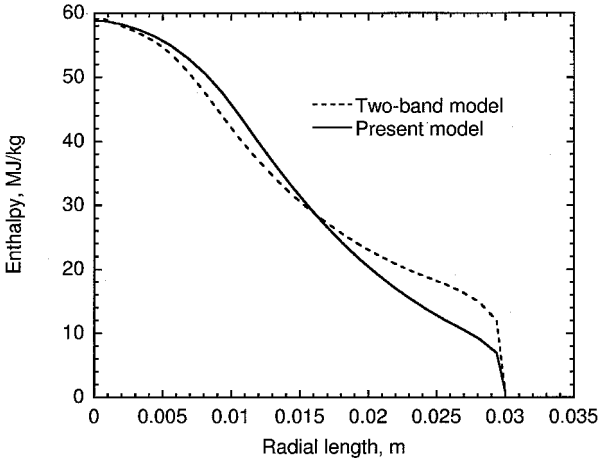

Fig. 6 Comparison of enthalpy distributions at the constrictor exit between two-band model and present model for case 4.

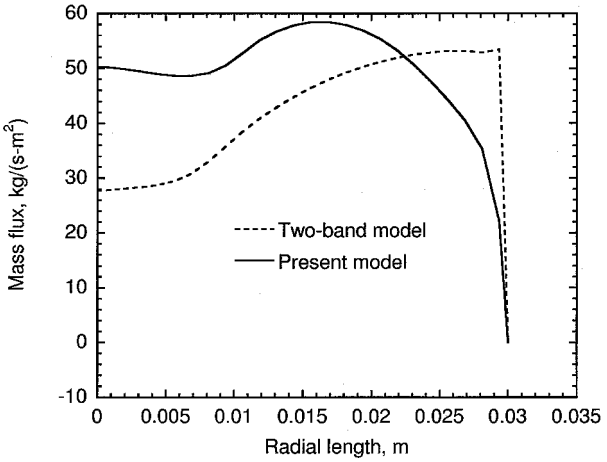

Fig. 7 Comparison of mass flux distributions at the constrictor exit between two-band model and present model for case 4.

was made with the original ARCFLO code for the same condition. The oscillatory behavior was seen in the original ARCFLO code. This observation implies that this grid problem is inherent with the ARCFLO code. The grid-dependence problem can be overcome if the ARCFLO code is converted into a computational fluid dynamics (CFD) code, such as ARCFLO2 (Ref. 16), because the well-established CFD principles will govern the grid-dependence of the solution. Such a conversion remains to be made in the future.

The radial enthalpy and mass-flux distributions are given in Figs. 6 and 7, respectively. Although the values of enthalpy near the wall by the PRG model are lower than those by the two-band model, the qualitative features between two results are the same. However the mass-flux distribution by the present method is quite different from that by the original method.

The calculated results for the mass-averaged enthalpy and the voltage drop from case 9 to 12 are summarized in Table 6. The profiles of temperature at the entrance to the constrictor for CO_2 flows are taken to be the same as those for airflows. The enthalpy distributions are calculated from the temperature and a given pressure. Enthalpy and temperature are presented in Fig. 8. A case of airflow is also calculated for the purpose of comparison. Because the enthalpy of formation of CO_2 is different from that of air by definition, the mass-averaged enthalpy shown in Table 6 has been corrected to bring it to the same reference point, that is, the zero point of enthalpy for CO_2 is set to be 0 K. The difference of the voltage drop and the mass-averaged enthalpy between CO_2 flow and airflow is small, although the mass-averaged enthalpy of CO_2 is (slightly) less than that of air. This means that the heating efficiency of CO_2 flow is nearly equal to that of air for the condition of the same electrical power input.

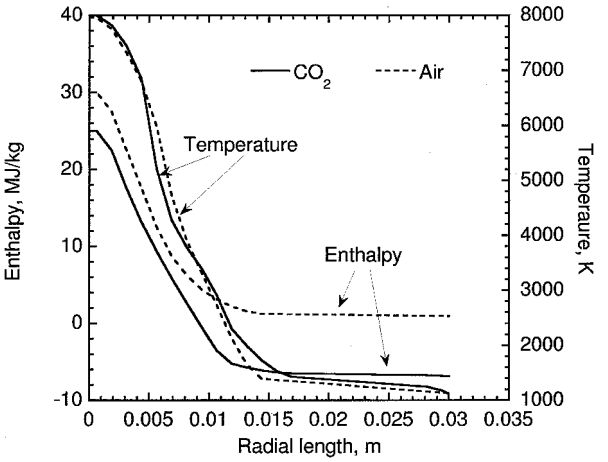

Fig. 8 Initial profiles of enthalpy and temperature for air and CO_2 flow.

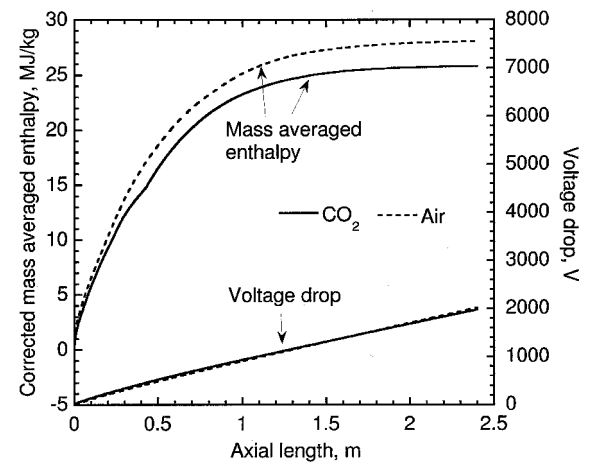

Fig. 9 Comparison of mass-averaged enthalpy and voltage drops for air and CO_2 flow for case 12.

The mass-averaged enthalpy and voltage drop for both CO_2 and airflow are shown in Fig. 9, and wall heat flux is shown in Fig. 10. The mass-averaged enthalpies are corrected values. It is seen in Fig. 10 that CO_2 and air behave similarly. In Fig. 10 the total heat flux for CO_2 gas is slightly higher than that for air at the downstream of the constrictor. However, it is not likely to exceed the operational limit designed for air. The fluctuation of the convective heat flux may be caused by the turbulence parameters used, as was pointed out for the case of air.

Figure 11 shows the calculated results of the carbon layer width and the effective wall temperature. The carbon layer width is finite and not negligible. Although it is thin, the layer supports a temperature difference of more than 1000 K to produce the surface temperature in excess of 2000 K. This rise in effective wall temperature is sufficiently high enough to affect the radiation calculation

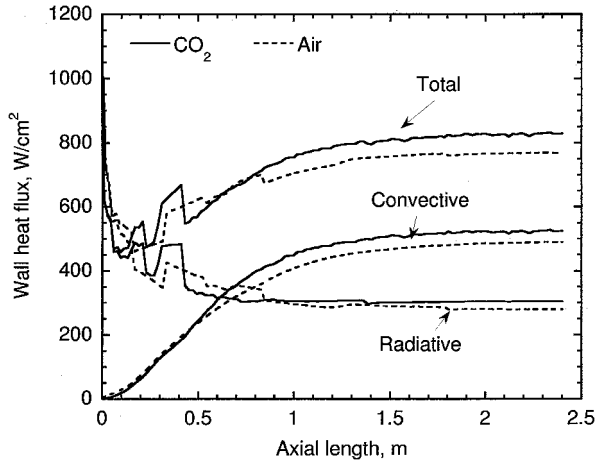

Fig. 10 Comparison of wall heat flux for air and CO_2 flow for case 12.

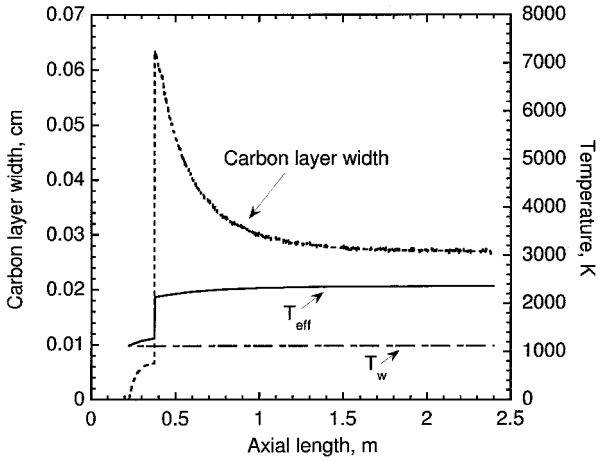

Fig. 11 Carbon layer depth and effective wall temperature for case 12.

near the wall. However, the absolute thickness is sufficiently small not to affect the cross-sectional area of the constrictor.

Concluding Remarks

The PRG model is successfully incorporated into the existing ARCFLO code for air and carbon dioxide flows. Turbulence is made stronger in the wall region in order to compensate for the decrease in the radiative transfer rate resulting from the change in the radiation model. For air cases the modification reproduces the experimental data at least as well as the original ARCFLO code. The grid-refinement study shows that the solutions are affected by the fineness of the grid. The cause of this problem cannot be verified in the present calculation. Such stability and convergence problems should be addressed in a future study in which the parabolic nature of the ARCFLO code is converted into the hyperbolic nature by using CFD method. Such a study is being carried out by the present authors. For the carbon dioxide case, for the same electrical power input as for air, the calculated mass-averaged enthalpy is almost the same as for air. Solid carbon layer is predicted to be developed for this case to a thickness of a few tenths of one millimeter, which raises the effective wall temperature substantially but does not affect the flow otherwise.

Acknowledgment

The authors would like to thank Chul Park for his suggestions and informative discussions.

References

[1]Horn, D. D., "Review of Existing Arc Jet Wind Tunnels," Lecture Notes, AIAA Short Course on Aerothermodynamic Facilities and Measurement, 1994.

[2]Mitsuda, M., Oda, T., Tagashira, S., and Shirai, H., "On the Characteristics of a Plasma Arc Heater for a High Enthalpy Wind Tunnel," AIAA Paper 97-2494, June 1997.

[3]Waston, V. R., and Pegot, E. B., "Numerical Calculations for the Characteristics of a Gas Flowing Axially Through a Constricted Arc," NASA TN D-4042, Oct. 1967.

[4]Nicolet, W. E., Shepard, C. E., Clark, K. C., Balakrishnan, A., Kesselring, J. P., Suchsland, K. E., and Reese, J. J., "Analytical and Design Study for a High-Pressure, High-Enthalpy Constricted Arc Heater," Arnold Engineering Development Center, AEDC-TR-75-74, Tullahoma, TN, July 1975.

[5]Sakai, T., Sawada, K., and Park, C., "Assessment of Planck-Rosseland-Gray Model for Radiating Shock Layer," AIAA Paper 97-2560, June 1997.

[6]Sakai, T., Sawada, K., and Park, C., "Calculation of Radiating Flowfield Behind a Reflected Shock Wave in Air," *Journal of Thermophysics and Heat Transfer*, Vol. 13, No. 1, 1999, pp. 42–49.

[7]Park, C., Howe, J. T., Jaffe, R. L., and Candler, G. V., "Chemical-Kinetic Problems of Future NASA Missions. II. Mars Entries: A Review," *Journal of Thermophysics and Heat Transfer*, Vol. 8, No. 1, 1994, pp. 9–23.

[8]Keston, A. S., "Radiant Heat Flux Distribution in a Cylindrically Symmetric Nonisothermal Gas with Temperature Dependent Absorption Coefficient," *Journal of Quantitative Spectroscopic and Radiative Transfer*, Vol. 8, 1963, pp. 419–434.

[9]Park, C., and Milos, F. S., "Computational Equations for Radiating and Ablating Shock Layers," AIAA Paper 90-0356, Jan. 1990.

[10]Bray, K. N. C., "Electron-Ion Recombination in Argon Flowing Through a Supersonic Nozzle," *The High Temperature Aspects of Hypersonic Flow*, Agardograph 68, edited by W. C. Nelson, Pergamon, 1964, pp. 67–87.

[11]Sakai, T., Sawada, K., and Mitsuda, M., "Application of Planck-Rosseland-Gray Model for High Enthalpy Arc Heaters," AIAA Paper 98-2838, June 1998.

[12]Park, C., *Nonequilibrium Hypersonic Aerothermodynamics*, Wiley, New York, 1990, pp. 119–143.

[13]Spitzer, L., *Physics of Fully Ionized Gases*, Interscience, New York, 1962, pp. 120–154.

[14]Gordon, S., and McBride, B. J., "Computer Program for Calculation of Complex Chemical Equilibrium Compositions, Rocket Performance, Incident and Reflected Shocks and Chapman-Jouguet Detonations," NASA SP-273, Feb. 1971.

[15]Perini, L. L., "Curve Fits of JANAF Thermochemichal Data," Johns Hopkins Univ., ANSP-M-5, Baltimore, MD, Sept., 1972.

[16]Kim, K. H., Rho, O. H., and Park, C., "Navier–Stokes Computation of Flows in Arc Heaters," *Journal of Thermophysics and Heat Transfer*, Vol. 14, No. 2, 2000, pp. 280–258.

[17]Roberts, R. C., *American Institute of Physics Handbook*, 2nd ed., McGraw-Hill, New York, 1963, Sec. 2, pp. 234–237.

[18]Riabov, V. V., "Approximate Calculation of Transport Coefficients of Earth and Mars Atmospheric Dissociating Gases," *Journal of Thermophysics and Heat Transfer*, Vol. 10, No. 2, 1996, pp. 209–216.

[19]Chase, M. W., Jr., Davies, C. A., Downey, J. R., Jr., Fruip, D. J., McDonald, R. A., and Syverud, A. N., "JANAF Thermochemical Tables, Third Edition, Parts 1 and 2," *Journal of Physical and Chemical Reference Data*, Vol. 14, Supplement No. 1, 1985, p. 671.

[20]Bueche, J. F., "Effect of Improvements and Uncertainties in Thermophysics and Temperature on Carbon Phenolic Heatshield Thermal Performance Predictions," AIAA Paper 77-787, June 1977.

[21]Park, C., "Evaluation of Real-Gas Phenomena in High-Enthalpy Aerothermal Test Facilities: A Review," *Journal of Thermophysics and Heat Transfer*, Vol. 11, No. 3, 1997, pp. 330–338.